

# Simulated effect of soil depth and bedrock topography on near-surface hydrologic response and slope stability

Cristiano Lanni,<sup>1,2\*</sup> Jeff McDonnell,<sup>2</sup> Luisa Hopp<sup>2</sup> and Riccardo Rigon<sup>1</sup>

<sup>1</sup> University of Trento, Environmental and Civil Engineering, Trento, Italy

<sup>2</sup> Oregon State University, Forestry Engineering, Corvallis, Oregon, USA

Received 14 June 2011; Revised 12 April 2012; Accepted 24 April 2012

\*Correspondence to: C. Lanni, University of Trento, Environmental and Civil Engineering, Trento, Italy. E-mail: cristiano.lanni@gmail.com

ESPL

Earth Surface Processes and Landforms

**ABSTRACT:** This paper explores the effect of hillslope hydrological behavior on slope stability in the context of transient subsurface saturation development and landslide triggering. We perform a series of virtual experiments to address how subsurface topography affects the location and spatial pattern of slip surface development and pore pressure dynamics. We use a 3D Darcy–Richards equation solver (Hydrus 3-D) combined with a cellular automata slope stability model to simulate the spatial propagation of the destabilized area. Our results showed that the soil–bedrock interface and in particular, bedrock depressions, played a key role in pore pressure dynamics, acting as an impedance for the downslope drainage of perched water. Filling and spilling of depressions in the bedrock surface microtopography induced localized zones of increased pressure head such that the development of pore-pressure fields—not predictable by surface topography—lead to rapid landslide propagation. Our work suggests that landslide models should consider the subsurface topography in order to include a connectivity component in the mathematical description of hydrological processes operating at the hillslope scale. Copyright © 2012 John Wiley & Sons, Ltd.

**KEYWORDS:** shallow landslide triggering; subsurface hydrological connectivity; bedrock topography; cellular automata models; landslide modelling

## Introduction

Shallow landslides and their translation into rapidly moving debris flows (Iverson *et al.*, 1997) are recognized as one of the major natural hazards for human life and activity (Olshansky, 1990; Schuster, 1995; Glade, 1998). Nevertheless, they are exceptionally difficult to predict with current models. The hydrological controls on soil mechanical behavior have been known for some time (Terzaghi, 1943). Shallow landslides are often induced by rainfall infiltration in a soil mantle overlying a less permeable bedrock. Rainfall infiltration reduces the soil shear strength by decreasing the positive effect of negative pore pressure on stability (Bishop, 1959; Campos *et al.*, 1994; Godt *et al.*, 2009) or by increasing the positive pore pressure values (Terzaghi, 1943). The failure surfaces may form within the weathered material (Lu and Godt, 2008; Hawke and McConchie, 2009), but often correspond to the point of contact between the soil and the less permeable bedrock, where a temporary perched water table may develop (Dietrich *et al.*, 2007; Baum *et al.*, 2010).

While hydrological models have been coupled with the infinite slope stability model (Montgomery and Dietrich, 1994; Wu and Sidle, 1995; Pack *et al.*, 1998; Borga *et al.*, 2002; Casadei *et al.*, 2003; Savage *et al.*, 2004; Baum *et al.*, 2008; Simoni *et al.*, 2008; Arnone *et al.*, 2011), almost all such models assume that the soil–bedrock interface is a simple topographic surface paralleling the soil surface. As a result,

none of the slope stability models have yet included an important new conceptual element derived from the hillslope hydrology literature: the filling and spilling of water perched at the soil–bedrock interface. Indeed the importance of moisture dynamics at the soil–bedrock interface has been widely acknowledged in hillslope hydrology (Weiler *et al.*, 2006). Recent hydrological analyses by several groups in several different hydrogeological settings (Spence and Woo, 2003; Buttle *et al.*, 2004; Tromp-van Meerveld and McDonnell, 2006b, Graham *et al.*, 2010; Spence, 2010) have shown that filling and spilling of microtopographic depressions in the bedrock topographic surface control the development and connectivity of patches of positive pore pressure. For the hillslope hydrologist, these patches and their downslope connectivity, form the precondition for resultant subsurface stormflow (Tromp-van Meerveld and McDonnell, 2006a). This behavior is now viewed as the dominant subsurface stormflow delivery mechanism whereby the existence of a threshold relationship between rainfall amount and hillslope outflow appears to be a common property of hillslope drainage (see review in Weiler *et al.*, 2006). For the slope stability modeler, these patches appear to be a key, unstudied part of the landslide initiation process with potential first-order hydrologic control on where a slip surface might be found.

Certainly, other sources of heterogeneity – related to soil cohesion, soil friction angle, soil permeability, root cohesion, and rainfall – may affect the location of shallow landslide events (Duan and Grant, 2000; Schmidt *et al.*, 2001; Minder

*et al.*, 2009). However, in this paper we focus solely on the role played by soil depth and bedrock topography, an aspect that has so far received very little attention in the context of hillslope stability, although it has been shown that failure location and size are largely controlled by the spatial structure of soil depth (Dietrich *et al.*, 2007).

So what do we know about fill and spill behavior? Recent model analysis by Hopp and McDonnell (2009) showed that the balance of filling and spilling on a given hillslope was primarily slope angle dependent. For shallow slopes, filling dominated spilling, whereby subsurface depressions acted to retain water ponded at the soil–bedrock interface. For steeper slopes, this ratio of upslope to downslope control shifted such that steep slopes were dominated by spilling, with much less filling. In terms of topographic representation of these processes, upslope accumulated area was the best proxy for filling, whereas downslope drainage efficiency (as defined by the downslope index of Hjerdt *et al.*, 2004) was the best proxy for spilling. In the slope stability context, the key feature of the fill and spill concept is not whole-slope subsurface stormflow activation, but rapidly connecting patches of isolated subsurface saturation (i.e. sub-meter scale pockets of positive pore pressure in microtopographic depressions at the soil bedrock interface) that grow to produce patches of saturation at scales relevant to rapid shear strength reduction (on the order of meters squared to several meters squared).

Here we explore for the first time, the effect of fill and spill development on slope stability in the context of subsurface patch saturation development and landslide triggering. Our overarching goal is to answer the question: how does bedrock topography influence the dynamics of pore pressure development and resulting triggering of shallow landslides?

We follow the approach of Weiler and McDonnell (2004) and present a number of virtual experiments where we explore the influence of the bedrock topography on the overlying pore pressure profile. We use the well known Panola hillslope hydrological research site (Freer *et al.*, 2002) as a virtual laboratory to explore how soil depth, slope inclination and other factors conspire to trigger shallow landslides. We then address a number of sub-questions using our virtual experiment approach:

- (1) How does the subsurface topography affect the location and spatial pattern of slip surface development?
- (2) How does local and slope-averaged slope angle influence maximum pore pressure and temporal and spatial extension of transient saturation at the soil bedrock interface?
- (3) How does rainfall amount and intensity affect development of positive pore pressure at the soil–bedrock interface of steep hillslopes?
- (4) How does bedrock topography influence the size and shape of the triggered area?

We build upon the work of Hopp and McDonnell (2009) where we use the 3D Richards equation solver, Hydrus 3-D (Simunek *et al.*, 2006), to quantify patterns of pore pressure development and 3D flow in porous media. We link this to a slope stability model that builds upon a modified version of the cellular automata model (CA) presented in Piegari *et al.* (2009). Our CA model simulates the spatial propagation of the destabilized area providing an estimation of the hillslope area on the verge of collapse.

## The Panola trench hillslope

We use the Panola hillslope as a shell for our virtual experiments. The Panola experimental hillslope has a slope angle of 13°, is 28 m wide and 48 m long and lies within the Panola Mountain Research Watershed (PMRW), located about 25 km southeast of

Atlanta, Georgia, USA, in the southern Piedmont. The site is described in detail by Tromp-van Meerveld and McDonnell (2006a, 2006b) and we refer the reader to those papers for further details. The downslope boundary of the Panola hillslope is formed by a 20 m wide trench. The upper boundary of the study hillslope is formed by a small bedrock outcrop. Soil depths on the study hillslope have been measured on a regular 2x2 m grid and linearly interpolated to a 1x1 m digital elevation model. The surface topography of the study hillslope is largely planar while the bedrock topography is very irregular, resulting in highly variable soil depth across the study hillslope ranging from 0 to 1.86 m with an average value of 0.63 m (Figure 2, upper left map).

The soil on the study hillslope is a sandy loam without clear structuring or layering, except for a 0.15 m deep organic-rich soil horizon. The soil is classified as the coarse, loamy, mixed thermic Typic Dystrochrepts from the Ashlar series. There are no observable differences in soil type across the study hillslope. The climate is humid and subtropical with a mean annual air temperature of 16.3 °C and mean annual precipitation of 1240 mm, spread uniformly over the year (NOAA, 1991). Rainfall tends to be of long duration and low intensity in winter, when it is associated with the passage of fronts, and of short duration but high intensity in summer, when it is associated with thunderstorms (Tromp-van Meerveld and McDonnell, 2006a). Overland flow is uncommon at PMRW and is observed only during very intense thunderstorms after extended dry periods. Even during these storms, overland flow was restricted to small areas and re-infiltrated within several meters.

## Methods

### The hydrological response model and the hillslope stability model

We used the Hydrus-3D hydrological model (Simunek *et al.*, 2006) to compute water movement in unsaturated/saturated soil and to provide the three-dimensional pore-pressure field input to our slope stability model. Hydrus 3-D can accommodate flow domains with irregular geometries like that of the Panola hillslope. It solves the Richards Equation (Richards, 1931):

$$C(\psi) \frac{\partial \psi}{\partial t} = \nabla \cdot \left( K(\psi) \vec{\nabla} (z + \psi) \right) \quad (1)$$

where  $C(\psi) = \frac{\partial \theta}{\partial \psi}$  is the hydraulic capacity [L<sup>-1</sup>],  $\psi$  [L] is the matric suction head,  $t$  [T] is the time,  $K$  [LT<sup>-1</sup>] is the hydraulic conductivity,  $z$  [L] is the elevation above a vertical datum,  $\nabla$  is the divergent operator, and  $\vec{\nabla}$  is the gradient operator.

For mechanical behavior of the Panola soils, we assumed a rigid and perfectly-plastic soil behavior. According to the modified Bishop's criterion (1959) proposed by Lu and Likos (2006), we define the soil-shear strength  $\tau$  [FL<sup>-2</sup>] as:

$$\tau = c' + [(\sigma - p_a) - \sigma^s] \cdot \tan \phi' \quad (2)$$

where  $c'$  [FL<sup>-2</sup>] is the effective soil cohesion,  $\sigma$  [FL<sup>-2</sup>] is the total stress,  $p_a$  [FL<sup>-2</sup>] is the pore-air pressure,  $\phi'$  is the effective soil frictional angle,  $\sigma^s$  is defined as the suction stress characteristic curve of the soil with a general functional form of:

$$\begin{aligned} \sigma^s &= -(p_a - p_w) \text{ if } (p_a - p_w) \leq 0 \\ \sigma^s &= f(p_a - p_w) \text{ if } (p_a - p_w) > 0 \end{aligned} \quad (3)$$

where  $p_w$  [FL<sup>-2</sup>] is the pore-water pressure. This criterion allowed the contribution of negative pore-water pressure (suction) on soil shear strength to be taken into account.

The suction stress characteristic curve,  $\sigma^s$ , can also be expressed in terms of effective saturation degree or normalized volumetric water content following Vanapalli *et al.* (1996):

$$\sigma^s = -\frac{\theta(\psi) - \theta_r}{\theta_{sat} - \theta_r} (p_a - p_w) = -S_e(p_a - p_w) \quad (4)$$

where  $S_e$  [–] is the relative saturation degree,  $\theta(\psi)$  [–] is the actual water content,  $\theta_{sat}$  [–] is the saturated water content, and  $\theta_r$  [–] is the residual water content.

We based our slope stability estimates on the calculation of the factor of safety  $FS$ . For hillslopes it is common to define the safety factor as the ratio between maximum retaining forces,  $F_r$ , and driving forces,  $F_d$ :

$$FS = \frac{F_r}{F_d} \quad (5)$$

Simply put, the slope is stable for  $FS > 1$ , while slope failure occurs when the critical state  $FS = 1$  (such that  $F_r = F_d$ ) is achieved. The infinite slope stability hypothesis has been widely applied in many investigations of natural slope stability (Montgomery and Dietrich, 1994; Wu and Sidle, 1995; Borga *et al.*, 2002; Van Beek, 2002; Casadei *et al.*, 2003; D'Odorico *et al.*, 2005; Lu and Godt, 2008) because of its relative simplicity, where the thickness of the soil mantle is much smaller than the length of the slope.

Assuming  $p_a = 0$  in Equations (2), (3) and (4), the factor of safety of an infinite slope model that accounts for saturated/unsaturated zones can be written as:

$$FS = \frac{2c'}{\gamma \bar{z} \sin(2\beta_i)} + \frac{\tan \phi'}{\tan \beta_i} + \frac{\gamma_w \psi}{\gamma \bar{z}} (\tan \beta_i + \cot \beta_i) \tan \phi' \quad \text{for } \psi \leq 0 \quad (6)$$

$$FS = \frac{2c'}{\gamma \bar{z} \sin(2\beta_i)} + \frac{\tan \phi'}{\tan \beta_i} + S_e(\psi) \frac{\gamma_w \psi}{\gamma \bar{z}} (\tan \beta_i + \cot \beta_i) \tan \phi' \quad \text{for } \psi > 0$$

where  $\beta_i$  [°] is the local slope angle,  $\bar{z}$  [L] is the vertical soil-depth, and  $\gamma_w$  and  $\gamma$  [FL<sup>-3</sup>] are the volumetric unit weight of water and soil, respectively.

Using the unstable locations provided by the infinite slope stability model as a starting point, we used a cellular automata (CA) model (see Bak *et al.*, 1987; Rodriguez-Iturbe and Rinaldo, 1997; Jensen, 1998 for a review) to propagate instability on our study hillslope.

CA is conceptually related to raster GIS because it models the space by tessellating it into regular, discrete locations and assigning attributes to each location. An individual cell can be viewed as a unique location within the grid. Raster GIS data can be associated with the states of the automaton and represent the spatial information on which the model works. A cell's state will change according to transition rules that apply simultaneously to every cell in the space. These rules are based on both the current state of the cell under study and also the state of its neighbors. CA models have been largely used to model landslide propagation for regional landslide characterizations that exhibit self-organized critical states (Avolio *et al.*, 2000; Clerici and Perego, 2000; Turcotte *et al.*, 2002; D'Ambrosio *et al.*, 2003; Iovine *et al.*, 2003; Guthrie *et al.*, 2007).

We modified the slope stability CA model of Piegari *et al.* (2009) for this study. Piegari *et al.* (2009) accounted for the effect of the triggering factor (i.e. rainfall) on the value of factor of safety ( $FS$ ) by introducing an empirical parameter  $\nu$  that controlled the rate at which all sites were driven towards instability. In our modified version of their CA model, we

accounted for rainfall effects on landslide triggering using pore pressure dynamics simulated by Hydrus 3-D. We adopt a scheme in which the solid and fluid sub-problems are uncoupled and the patterns of  $FS$  are re-initialized at each time step on the base of the  $FS$  configuration provided by the infinite slope stability model. More specifically, when a raster-cell  $i$  becomes unstable (i.e.  $FS_i \leq 1$  according to the infinite slope stability model), it affects, via a chain reaction, the stability of the eight neighboring cells  $i_{nn}$ , by reducing their driving forces,  $F_d^{i_{nn}}$ , by a fraction  $\lambda$  of the driving forces of the destabilized cell  $i$ ,  $F_d^i$ :

$$FS_{i_{nn}} = \frac{F_r^{i_{nn}}}{F_d^{i_{nn}} + \frac{1}{8} \lambda F_d^i} \quad \text{with } nn = 1, \dots, 8 \quad (7)$$

where  $FS_{i_{nn}}$  and  $F_r^{i_{nn}}$  with  $nn = 1, \dots, 8$  are the safety factors and the retaining forces of the eight neighboring cells, respectively.

In Equation (7) the fraction  $\frac{1}{8}$  indicates that the destabilizing forces  $F_d^i$  of the unstable cell  $i$  are redistributed equally among the neighboring cells  $i_{nn}$ . The parameter  $\lambda$  is a parameter that determines the degree of conservation of the system.  $\lambda = 0$  means that the system is completely dissipative (i.e., the destabilized locations do not affect the stability of the neighboring cells), while  $\lambda = 1$  means that the system is completely conservative (i.e., the destabilizing forces of destabilized locations are completely transferred to neighboring cells). We assume  $0 < \lambda < 1$  by considering a non-conservative case, since many complex dissipative phenomena can contribute to stress transfer processes (Fredlund and Rahardjo, 1993). The chain reaction continues until no unstable locations are generated, according to the flow chart of Figure 1.

This simplified model was used to propagate instability and to provide an estimation of the most likely landslide initiation zones on the hillslope.

## Hydrological and mechanical characterization

Hopp and McDonnell (2009) evaluated Hydrus 3-D's ability to represent measurements of pore-pressure recorded by tensiometers at several points in the Panola hillslope (detailed information on the field data can be found in Freer *et al.*, 2002). We used the same soil water retention and hydraulic conductivity functions as Hopp and McDonnell (2009). These

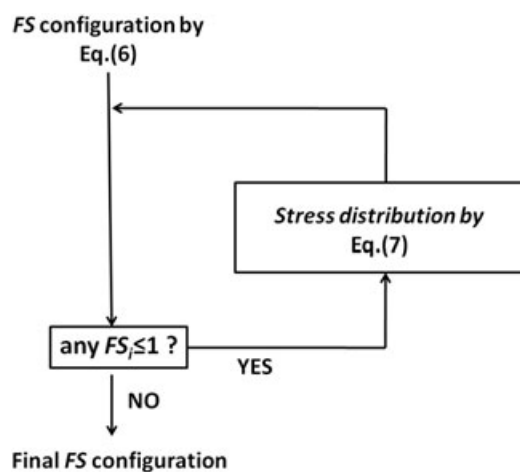


**Figure 1.** Flow chart of the cellular automata model. The stress is propagated until no new unstable locations are generated. The final  $FS$  configuration gives an estimation of the most likely hillslope portion to be affected by landslide activation.

are described using the van-Genuchten-Mualem model (van Genuchten, 1980):

$$S_e = \frac{\theta(\psi) - \theta_r}{\theta_{sat} - \theta_r} = \left[ \frac{1}{1 + (\alpha\psi)^n} \right]^{1-\frac{1}{n}} \quad (8)$$

$$K(\psi) = K_{sat} S_e^{0.5} \left[ 1 - \left( 1 - S_e^{n/n-1} \right)^{1-\frac{1}{n}} \right]^2 \quad (9)$$

where  $\alpha$  [ $L^{-1}$ ] is a parameter that depends approximately on the air-entry (or air-occlusion) suction,  $n$  [–] is a parameter that depends on the soil pore-size distribution,  $K_{sat}$  [ $LT^{-1}$ ] is the saturated hydraulic conductivity.

The soil mantle was divided into three layers to account for the observed reduction of saturated hydraulic conductivity  $K_{sat}$  in the profile. Saturated hydraulic conductivity of the bedrock saprolite was approximated based on measured values reported in Tromp-van Meerveld *et al.* (2007). Table I shows the hydrological parameters used in this study to characterize both soil and the bedrock material of the Panola hillslope. For our virtual experiments, we set the saturated hydraulic conductivity at the contact between soil and bedrock to be three orders of magnitude less than the soil  $K_{sat}$ .

Both the water retention function and the hydraulic conductivity function of the soil material and bedrock saprolite exhibit a steep slope near zero pressure head. In particular, the soil hydraulic conductivity  $K(\psi)$  increases drastically near zero pressure head in a short range of suction head  $\psi$  (about 0.5 m).

We used empirical relationships (by Terzaghi *et al.*, 1996) to estimate the effective frictional angle ( $\phi' = 34^\circ$ ) and the effective cohesion ( $c' = 0$  kPa) of the sandy loam soil of Panola hillslope. The bedrock layer was considered stable in our experiments because of the good mechanical characteristic of the saprolite rock.

## Virtual experiment design

The geometrical domain of Panola hillslope was implemented in Hydrus 3-D where a finite element mesh of triangular prisms with 35600 nodes and 64638 3D-elements was generated. On this geometry, we conducted eight experiments that included three different slope angles  $\beta$  ( $13^\circ$ , i.e. the original Panola hillslope inclination,  $20^\circ$ , and  $30^\circ$ ) and four different rainfall events. Each rainfall event was spatially and temporally uniform. These events were characterized by the same cumulative rainfall, but different distribution in time (i.e. different values of rainfall intensity and duration). Two rainfall scenarios (*long-rainfall* and *short-rainfall* in Table 2) were selected for the virtual experiments with the lower slope angles ( $\beta = 13^\circ$  and  $\beta = 20^\circ$ ). Two events (*very long-rainfall*, and *very short-rainfall* in Table 2) were also analyzed in the steepest hillslope case ( $\beta = 30^\circ$ ).

Our three hillslope inclinations ( $\beta = 13^\circ$ ,  $\beta = 20^\circ$ , and  $\beta = 30^\circ$ ) allowed us to investigate how the overall slope angle influences the maximum pore-pressure values, the spatial extension and

level of connectivity of patterns of transient saturation at the soil–bedrock interface, and the temporal persistence of these. Despite these overall slope angle comparisons, the local slope values,  $\tan \beta_i$ , of the bedrock topography (i.e. at the soil–bedrock interface) in any given pixel was highly variable and often larger than the overall slope angle  $\tan \beta$ . For example,  $\beta_i$  ranged from  $6^\circ$  to  $57^\circ$  at the steepest ( $\beta = 30^\circ$ ) hillslope configuration. Hence, because of the soil mechanical properties of the sandy loam soil ( $\phi' = 34^\circ$  and  $c' = 0$  kPa) and according to Equation (6), some points would achieve instability under positive pore pressure (i.e. where  $\tan \beta_i < \tan \phi'$ ) and some others would achieve instability under negative pore pressure (i.e. where  $\tan \beta_i > \tan \phi'$ ).

Initial conditions for our virtual experiments were set to a relatively dry state (with low unsaturated hydraulic conductivity values) which reproduces the antecedent soil-moisture condition generally observed at the Panola hillslope (Tromp-van Meerveld *et al.*, 2007) before a rainfall event. The initial mean soil-water content was  $\theta = 0.32 \text{ cm}^3 \text{ cm}^{-3}$ , with initial pressure head  $\psi$  ranging from  $-1.0$  to  $-0.7$  m linearly distributed with depth. This relatively dry state ensured that: (i) numerical results were not affected by the unbalanced initial conditions, such that modification in pore-pressure regime was only due to the effect of rain infiltration; (ii) the factor of safety,  $FS$ , of the steepest hillslope configuration ( $\beta = 30^\circ$ ) was greater than 1 in each point of the hillslope before of the beginning of rainfall. For boundary conditions, we assumed an atmospheric boundary (i.e. rainfall rate) at the soil surface (i.e. upper boundary of the numerical domain), a potential seepage face boundary at the downslope end of the hillslope (the face was treated as a prescribed pressure head boundary with  $\psi = 0$ , while the unsaturated part was treated as a no-flux boundary), a free drainage boundary at the bottom boundary of the numerical domain (by imposing a unit gradient of the total head so that the flux was equal to the hydraulic conductivity for any particular pressure head at given time), and a no-flux boundary at the upslope and side boundaries.

## Results

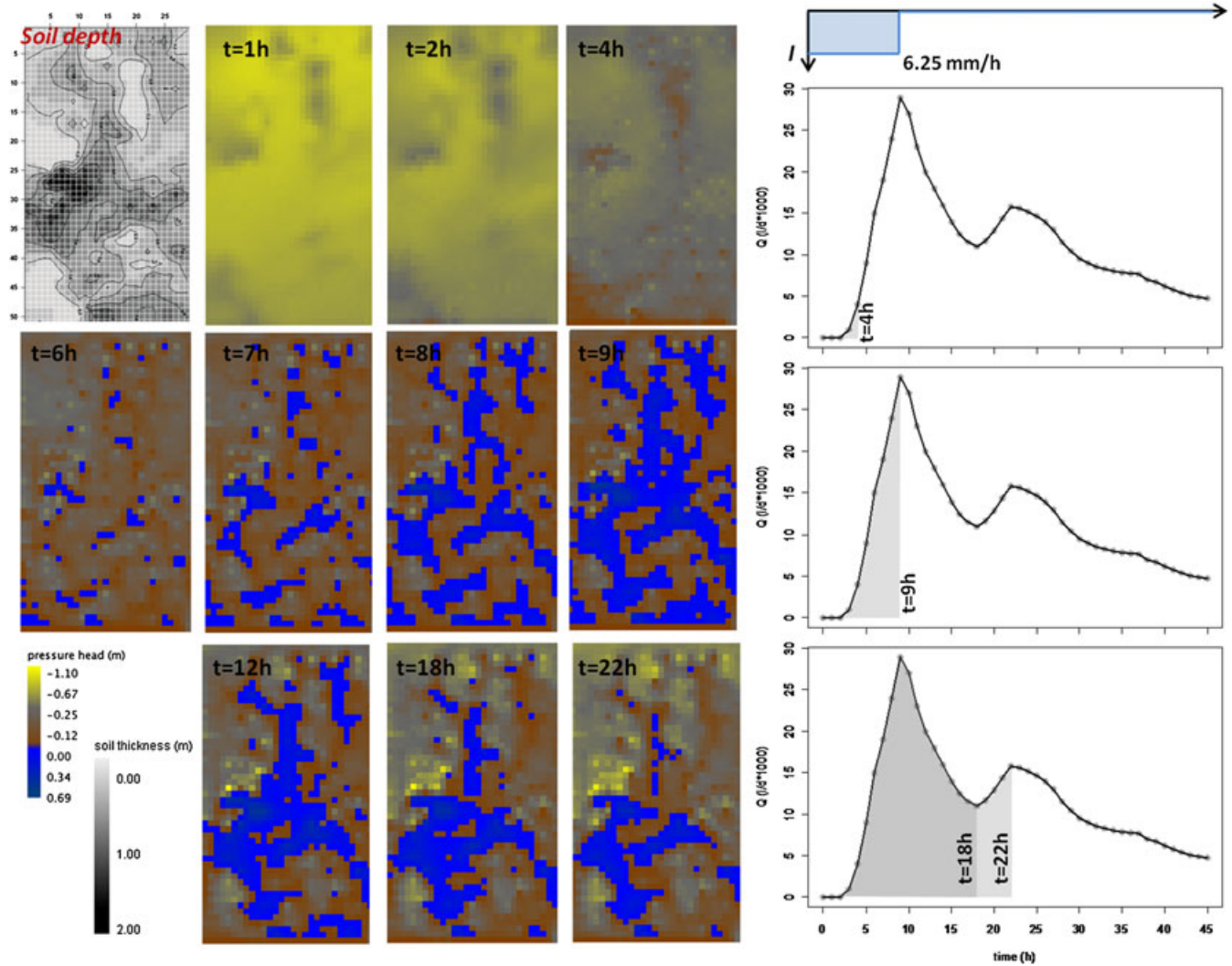
### The role of bedrock topography on pore pressure development and integrated hydrological response

Figure 2 shows the temporal evolution of pressure head at the soil–bedrock interface for the base case  $13^\circ$ -Panola hillslope during the *long-rainfall* event ( $I = 6.25 \text{ mm h}^{-1}$ ,  $D = 9 \text{ h}$  in Table II). Well-connected patches of saturation developed after 9 h from the onset of rainfall. The mid-slope zone was characterized by the main bedrock depression (the soil-depth map is shown in the upper left corner of Figure 2), and exhibited the highest pore-pressure values (with a maximum value of 0.69 m). The hillslope hydrograph from the slope base is also shown in Figure 2 (right-hand side), where the shaded portions correspond to the time periods of pore pressure development. The hillslope hydrograph shows a double peak: the first at the end of the long-rainfall event (9th hour), the second 13 h after the end of this rainfall (22nd hour). The minimum value of

**Table I.** Average soil thickness  $\bar{\Delta z}$  and hydrological parameters of the soil and saprolite bedrock layers of Panola Hillslope (from Hopp and McDonnell, 2009).

Material	$\bar{\Delta z}$ (cm)	$\theta_r$ (–)	$\theta_{sat}$ (–)	$\alpha$ ( $\text{cm}^{-1}$ )	$n$ (–)	$K_{sat}$ ( $\text{m s}^{-1}$ )
Soil	15	0.28	0.475	0.04	2	$10^{-3}$
	10	0.28	0.46	0.04	2	$4 \cdot 10^{-4}$
	38	0.325	0.45	0.04	2	$1.8 \cdot 10^{-4}$
Bedrock	-	0.30	0.45	0.0325	2	$1.7 \cdot 10^{-7}$





**Figure 2.** Patterns of transient saturation at the soil–bedrock interface of the original 13° Panola hillslope for distinct timesteps in the hillslope hydrograph (shaded righthand side of the figure) for several hours during the *long-rainfall* event. The blue zones represent the patches of transient saturation (perched water table), the yellow, grey and brown colors identify variably unsaturated soil conditions. Flow is concentrated in the mid-slope, which exhibits the highest pore pressure values. The soil depth map is inserted in the upper lefthand corner for reference. This figure is available in colour online at [wileyonlinelibrary.com/journal/espl](http://wileyonlinelibrary.com/journal/espl)

discharge between these two peaks is localized around the 18th hour (9 h after the end of the event). The second peak is due to the spilling of water from the main-bedrock depression that was filled during the drainage following the initial rainfall burst.

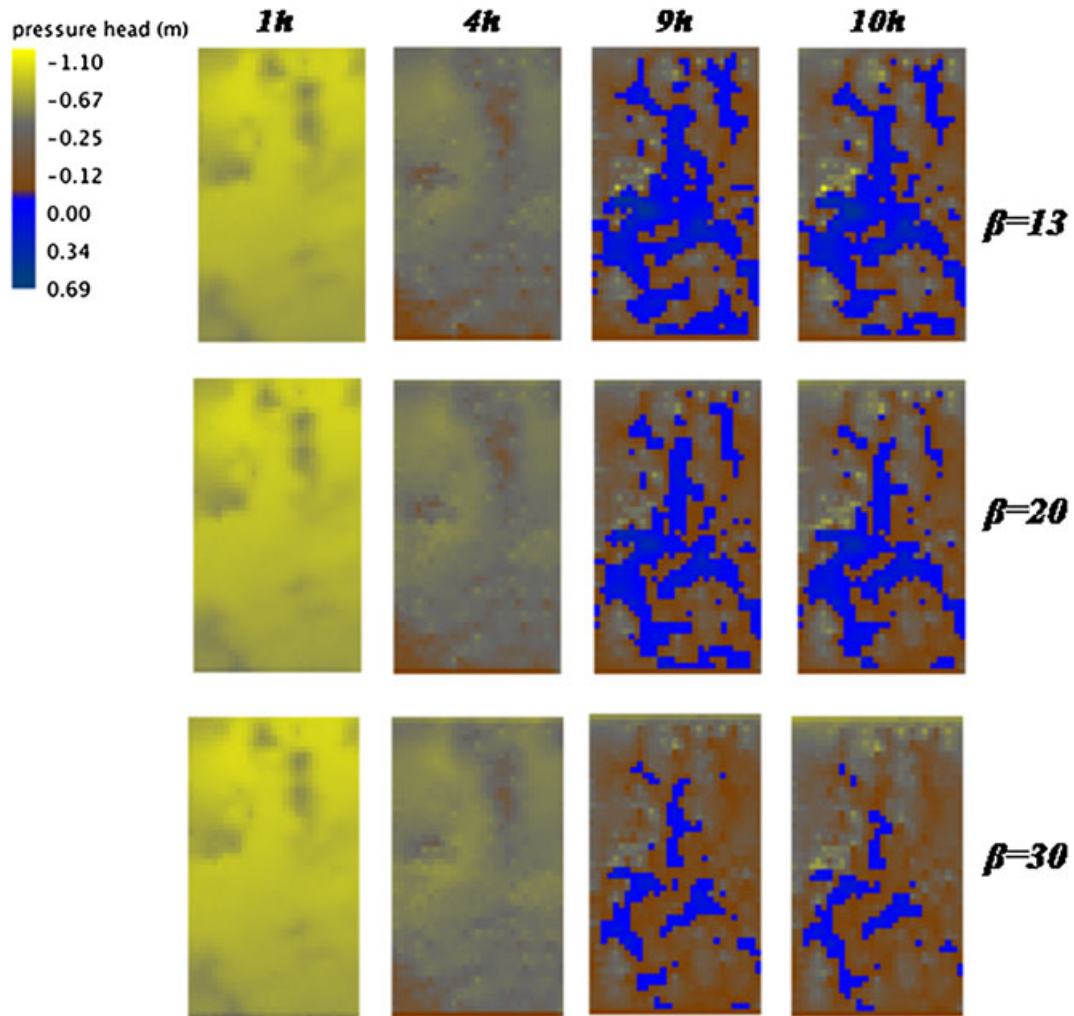
**Relation between hillslope gradient and spatio-temporal extent of transient saturation at the soil–bedrock interface**

Figure 3 describes the relation between hillslope gradient and spatio-temporal extent of transient saturation at the soil–bedrock interface for the *long-rainfall* event ( $I=6.25 \text{ mm h}^{-1}$

and  $D=9 \text{ h}$ ). An increase in overall slope angle  $\beta$  lead to a general decrease in the extension and connectivity of saturated areas and their temporal persistence at the soil–bedrock interface. This finding is consistent with Hopp and McDonnell (2009). Despite the slope angle influence, the maximum value of pressure head (0.69 m) was not affected by the slope inclination. During the first stage of rainfall (at approximately 4–5 h), pore pressure maps at the soil bedrock interface of 13°, 20° and 30° slope angles showed similar patterns (first and second columns in Figure 3). The maps of pore pressure resemble the map of soil depth (shown in the upper left corner of Figure 2) with areas characterized by the thinnest soils responding first to the precipitation input.

**Table II.** Hillslope angles and rainfall event features used in the virtual experiments. I = rainfall intensity; D = rainfall duration.

		Rainfall event			
		Very short	Short	Long	Very long
		$I=20 \text{ mm h}^{-1}$ $D=3 \text{ h}$	$I=12 \text{ mm h}^{-1}$ $D=5 \text{ h}$	$I=6.25 \text{ mm h}^{-1}$ $D=9 \text{ h}$	$I=5 \text{ mm h}^{-1}$ $D=12 \text{ h}$
Overall slope angle $\beta$	13°		•	•	
	20°		•	•	
	30°	•	•	•	•



**Figure 3.** Maps of pore pressure at the soil bedrock interface of the original 13° Panola hillslope (first row), and the modified 20° and 30° Panola hillslopes (second and third rows, respectively) for the *long-rainfall* event. Maps of pore-pressure are quite similar during the first stage of rainfall (the maps of 1st hour and 4th hour are showed in the first and second columns, respectively), while the overall inclination significantly affects the dynamic of pore pressure in the second stage of rainfall (the maps of 9th hour and 10th hour are showed in the third and fourth columns, respectively) when lateral flow becomes relevant. This figure is available in colour online at [wileyonlinelibrary.com/journal/esp](http://wileyonlinelibrary.com/journal/esp)

Figure 4(a) shows the temporal evolution of the transient saturation area at the soil–bedrock interface for the three slope angles during the *long-rainfall* event. The size of saturated area is expressed in terms of percentage of the total hillslope area. For all the investigated hillslope inclinations, perched water table developed shortly after 4–5 h from the beginning of the rainfall. The maximum size of saturated area reached 40% of the total hillslope area for the 13° hillslope, and 13% of the total hillslope area for the 30° hillslope. The time of persistence of this transient saturation was drastically reduced for the steepest hillslope. In fact, while the original 13° Panola hillslope still exhibited transient water-table at the soil–bedrock interface after 3 days of drainage, only 50 h and 28 h of drainage were necessary to dissipate positive pressure heads at the soil–bedrock interface for the modified 20° and 30° hillslopes, respectively.

In Figure 4(b), the average value of positive pore pressures developed at the soil–bedrock interface is plotted against the percentage of subsurface saturated area. The maximum size of saturated area at the soil–bedrock interface of the original 13° hillslope was achieved at the end of the event (9th hour). However, the average value of positive pore pressures continued to increase after the end of the event with the concomitant decrease of saturated area. The average value of positive pore pressures and saturated area extension both

decreased from the 14th hour onwards. The same behavior was also observed for the modified 20° and 30° hillslopes (with reduced time-lag between maximum saturated area and maximum value of average value of positive pore pressures), and for the other rainfall events (Table II) analyzed.

### When does slope angle affect the dynamics of subsurface flow and pore pressure development?

Pore-pressure rise at the soil–bedrock interface was inversely related to soil depth during the first hours of rainfall for all the three hillslope inclinations analyzed. During this first phase, rain infiltration was strictly vertical and no differences were found for the three hillslope angles analyzed ( $\beta = 13^\circ, 20^\circ, 30^\circ$ ). Figure 4(c) shows the evolution of the variance of the values of pressure head at the soil–bedrock interface  $\sigma_{\psi}^2(t)$  during the *long-rainfall* event.  $\sigma_{\psi}^2(t)$  is defined as follow:

$$\sigma_{\psi}^2(t) = \frac{1}{N} \sum_{i=1}^N (\psi_i(t) - \bar{\psi}(t))^2 \quad (10)$$

where  $N$  is the total number of nodes of the numerical domain at the soil–bedrock interface (1479 points),  $\psi_i [L]$  is the value of

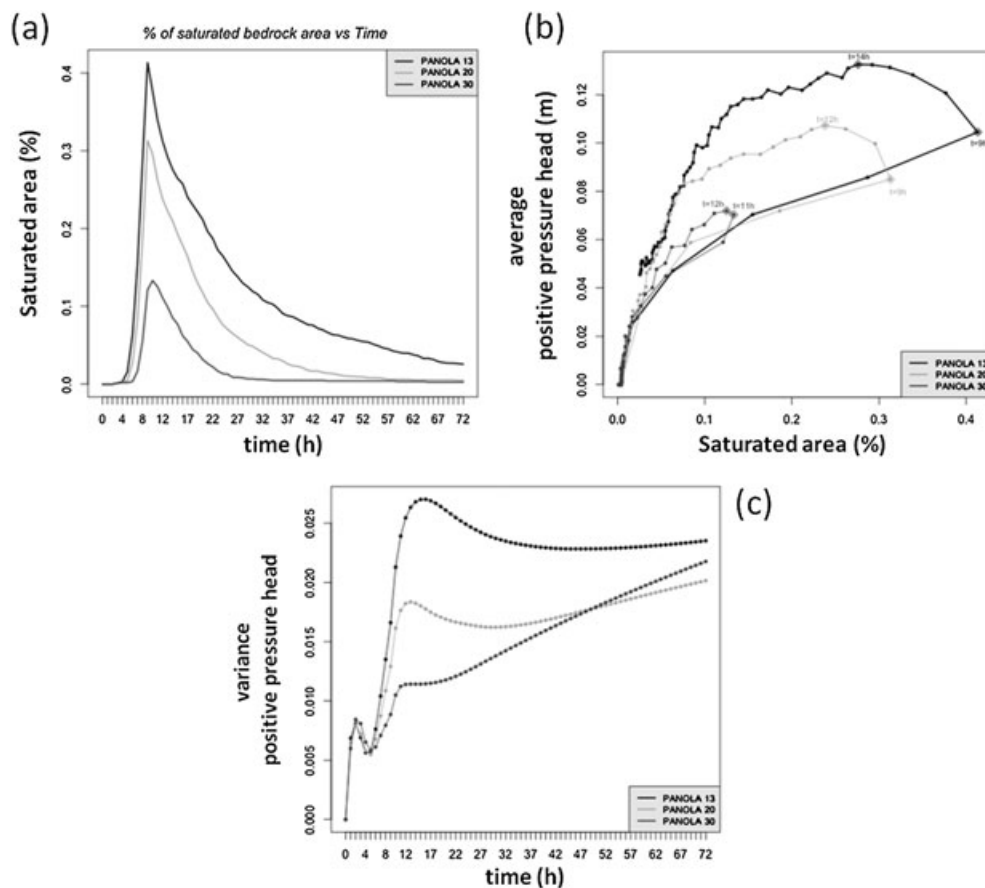


**Figure 4.** Saturated area and pressure head response for the *long-rainfall* event. (a) Temporal evolution of saturated area at the soil–bedrock interface of the original 13° and modified 20° and 30° Panola hillslopes during the *long-rainfall* event. (b) Dynamics of the mean value of positive pressure head versus percentage of saturated area at the soil–bedrock interface for the three Panola hillslope angles analyzed. (c) Temporal evolution of the variance  $\sigma_{\psi}^2$  of the values of pressure head recorded at the soil–bedrock interface for the three slope angles investigated.

pressure head at node  $i$ ,  $\bar{\psi} = \frac{1}{N} \psi_i$  is the average value of pressure head at the soil–bedrock interface, and  $t$  [T] is a generic time.

Equation (10) describes how much localized pore pressure values deviate from the average value of pressure head at the soil–bedrock interface. Therefore, it provides a measure of the spatial variability of pore pressure during and after the rainfall event. The initial value of the variance of pressure head at the soil–bedrock interface,  $\sigma_{\psi}^2(t=0)$ , was zero because all the nodes were characterized by the same pore-pressure value before the beginning of the *long-rainfall* event.  $\sigma_{\psi}^2(t)$  increased after the beginning of the event, indicating a different response of the bedrock-points to the rainfall input. The  $\sigma_{\psi}^2(t)$  of the three hillslope angles investigated (13°, 20°, and 30°) were very similar until the 5th rainfall-hour.  $\sigma_{\psi}^2(t)$  then diverged in the successive phases of the rainfall event. Hence, the hillslope gradient affected the pore pressure dynamics in the second phase of rainfall (4–5 h after rainfall commencement). In particular, the lower the overall hillslope angle  $\beta$ , the higher the variance of pressure head recorded at the soil–bedrock interface. This was basically related to the different (lateral) subsurface flow velocities in dissipating the positive pore pressure during the second phase of rainfall and after the end of the rainfall event.

All the investigated slope angles showed a double peak in the shape of  $\sigma_{\psi}^2(t)$  (Figure 4(c)). The second peak occurred always after the end of the event (15th hour, 13th hour, and 12th hour for the 13°-, 20°-, and 30°-Panola hillslope, respectively).

Figure 5 shows the maps of pressure head at the soil–bedrock interface for the modified 30° Panola hillslope during the *short-rainfall* ( $I=12 \text{ mm h}^{-1}$ ,  $D=5 \text{ h}$ ) and the *long-rainfall* ( $I=6.25$

$\text{mm h}^{-1}$ ,  $D=9 \text{ h}$ ) events. The maps are arranged in order of increasing amounts of cumulative rainfall. For both the *short-* and *long-rainfall* events a threshold of about 35 mm of rainfall was necessary to generate measurable spots of transient saturation at the soil–bedrock interface. Once this threshold was exceeded, a rapid propagation of transient saturation extent was then observed. The rainfall intensity  $I$  affected the temporal dynamics of this process but, irrespective of rainfall intensity, similar patterns of pore pressure were observed for the same total rainfall amount.

### Linking subsurface hydrology and landslide triggering

The pore pressure values provided by Hydrus 3-D were used to compute the factor of safety  $FS$  in each soil-pixel by applying the infinite slope stability model developed in Equation (6). This allowed calculation of the safety factor at each depth of the discretized domain. Only the steepest hillslope scenario ( $\beta=30^\circ$ ) was affected by conditions of instability (i.e. raster cells where the factor of safety  $FS$  dropped below 1). In particular, the slip surface (i.e. the depth of failure) was always localized at the soil–bedrock interface where  $FS$  first dropped below 1.

The CA model (Figure 3 and Equation (7)) was used to redistribute the driving forces of the unstable pixels to the neighboring regions within the hillslope domain and thus outline the hillslope zones on the verge of collapse. Figure 6 shows the patterns of unstable points for the 30°-hillslope at several times during the *long-rainfall* event. Red points represent unstable locations provided by the infinite slope stability model (Equation (6)). The black points are ones that



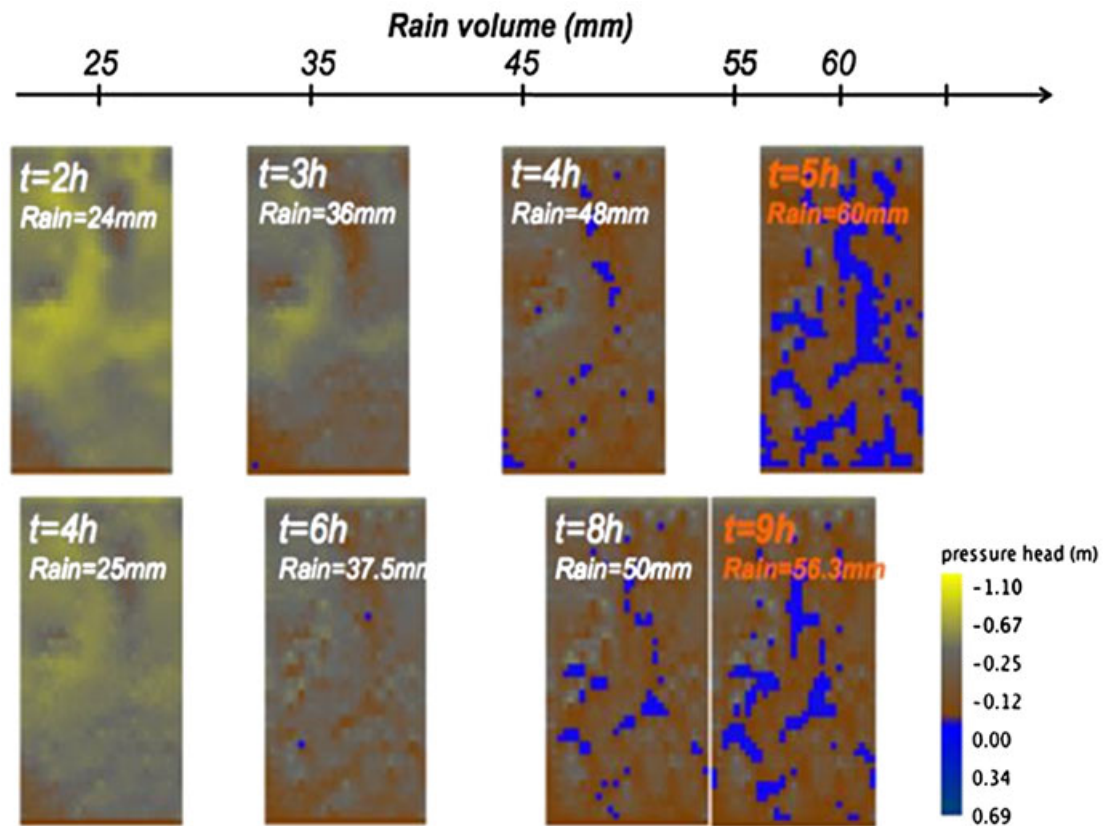


**Figure 5.** Maps of pore-pressure at the soil–bedrock interface of the modified 30°-Panola hillslope during the short-rainfall (top) and long-rainfall (bottom) events. Patterns of pore pressure are similar when the same value of cumulative rainfall has been achieved. This figure is available in colour online at [wileyonlinelibrary.com/journal/espl](http://wileyonlinelibrary.com/journal/espl)

become unstable when the driving forces of the destabilized locations are redistributed to the neighboring cells (Equation (7)). The patterns of instability were evaluated by using four different values of the failure propagation rate  $\lambda$  (i.e. the percentage of driving forces redistributed to the neighbors): 0.2, 0.4, 0.6 and 0.8.

Maps of instability in Figure 6 show two large clusters of instability with centers localized approximately 25 and 45 m downslope from the crest of the hillslope. Patterns of instability did not exhibit significant differences during the first rainfall hours and  $\lambda$  had only a small effect on where failure occurred (i.e. the maps in the 1st, 2nd, and 3rd columns in Figure 6 are very similar). On the other hand, instability spread very quickly in the second phase of rainfall (approximately 6–7 h after the onset of rainfall) especially when the higher values of  $\lambda$  ( $\lambda=0.6$  and  $\lambda=0.8$ ) were used to run the CA model. This threshold-like expansion behavior was also observed for the other rainfall events analyzed (*very short*-, *short*-, and *very long-rainfall* events in Table II), where the time at which the threshold expansion behavior was observed decreased with increasing rainfall intensity.

Figure 7 shows that instability spread very quickly when a cumulative rainfall of 30–35 mm was achieved, irrespective of rainfall intensity. Once this rain amount was exceeded a rapid propagation of instability was then observed. This precipitation threshold was similar for all the values of  $\lambda$  considered.

## Discussion

Many of today's popular landslide initiation models used to map landslide triggering assume that the ground surface topography is a good proxy to describe subsurface pore pressures and flow path dynamics or to characterize the initial conditions

for soil-water storage prior to rainfall events (Baum *et al.*, 2008). These models generally use the DEM of the ground surface to compute a steady-state (Montgomery and Dietrich, 1994; Wu and Sidle, 1995; Pack *et al.*, 1998) or a 'quasi-dynamic' wetness index (Borga *et al.*, 2002; Casadei *et al.*, 2003) where it is assumed that the specific (steady-state or time-variable) upslope area derived from the surface topography is a surrogate measure of subsurface flow in response to a rainfall of specified duration. The subsurface flow paths (i.e. the drainage directions) are then derived from DEM analysis and the land surface slope is used as a substitute for the slope of the subsurface hydraulic gradients.

Our results showed that subsurface topography, not surface topography, controls the development of perched water table during rainfall events and that bedrock depressions are the zones primarily responsible for localized pore pressure increases. These findings are consistent with the preponderance of evidence from many hydrological study hillslopes around the world (as reviewed in Weiler *et al.*, 2006). The filling and spilling of water in this zone has a first order effect on the generation of shallow landslide triggering.

## On the relation between bedrock topography and the development of positive pore pressure

The bedrock topography induced the development of positive pore pressure at the soil–bedrock interface. Filling and spilling of water in this zone determined the temporal evolution and the connectivity of zones of transient saturation at the soil–bedrock interface at the Panola hillslope. Rain water infiltrated vertically through the soil profile during the first stage of rainfall due to the high infiltration soil capacity of the Panola-soil. The



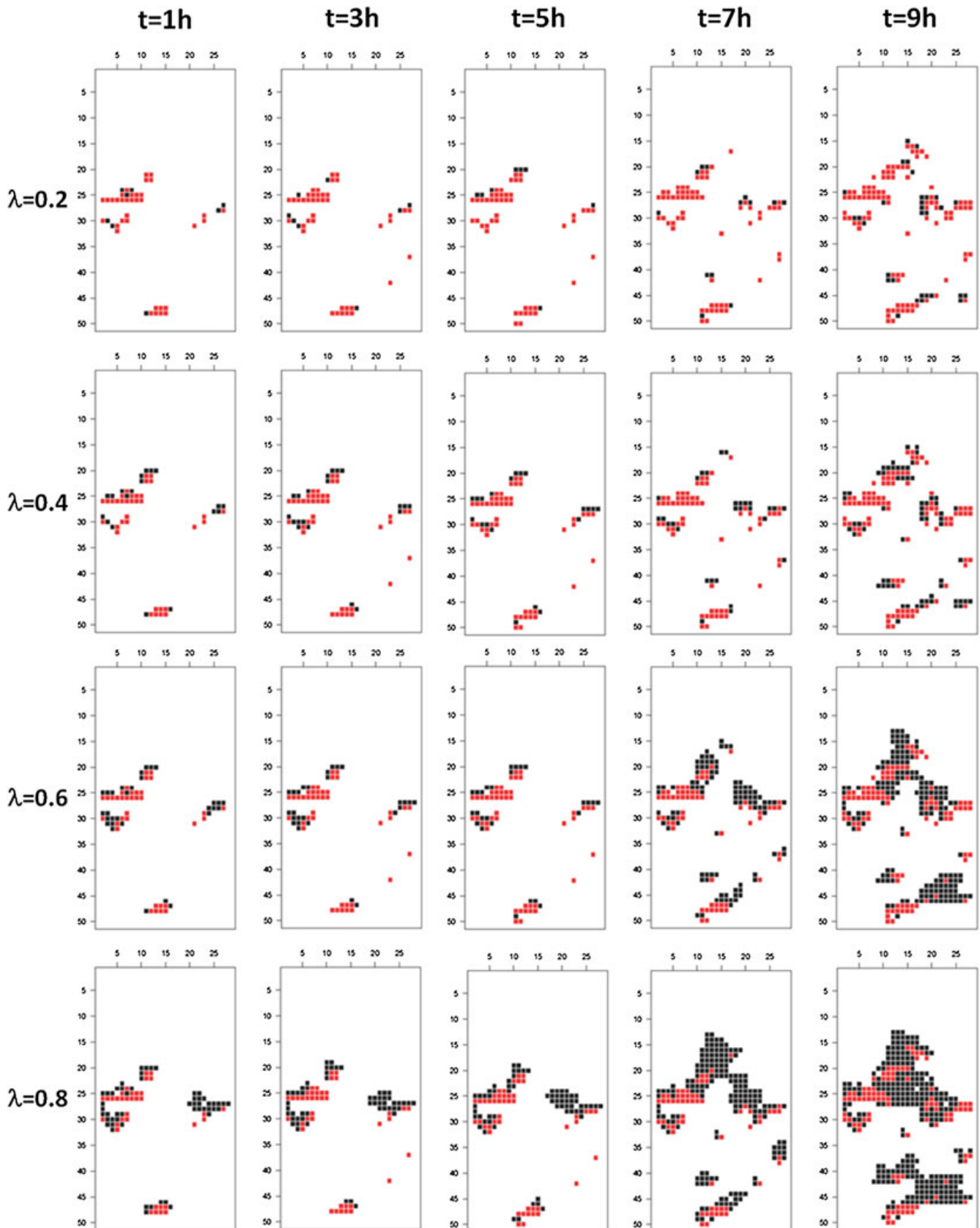


**Figure 6.** Temporal patterns of unstable locations generated by the cellular automaton (CA) model for four different values of  $\lambda$  (0.2, 0.4, 0.6, and 0.8 on the first, second, third and fourth row, respectively). The *long-rainfall* event case ( $I=6.25 \text{ mm h}^{-1}$ ,  $D=9 \text{ h}$ ) is shown here. In red are the points classified unstable by the infinite slope stability model (Equation (6)). The black points are the ones that become unstable when the driving forces of the destabilized locations are redistributed to the neighboring cells (Equation (7)). Rapid failure propagation is observed for high values of  $\lambda$  ( $\lambda=0.6$  and  $\lambda=0.8$ ) during the second stage of rainfall event (i.e. after 5 h from rainfall beginning). This figure is available in colour online at [wileyonlinelibrary.com/journal/espl](http://wileyonlinelibrary.com/journal/espl)

first bedrock points to respond to the precipitation input were those with the thinnest soil above the bedrock level, where a temporary perched water table developed and water began to

move laterally. The initially fragmented patches of transient saturation became more connected as the water table rose high enough so that water spilled then over the ridges of isolated

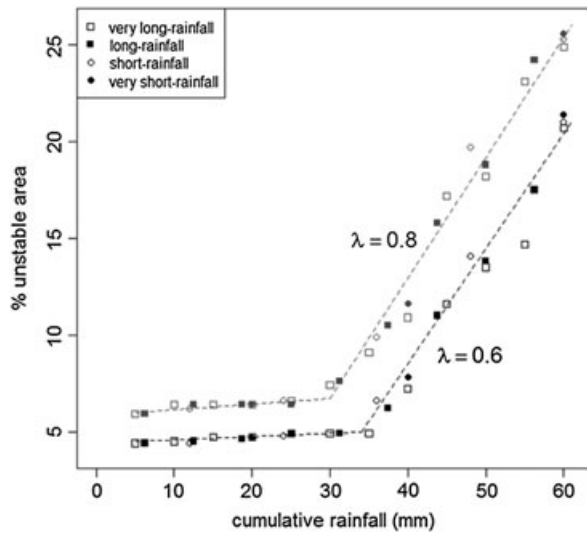


**Figure 7.** Cumulative rainfall against percentage of unstable area provided by the CA model for all the rainfall events analyzed. Instability spread very quickly when a cumulative rainfall of 30–35 mm was exceeded.

bedrock micro-depressions. The main bedrock depression on the midslope (see the upper left map in Figure 2) represented a major fill zone and was responsible for the slope-wide increase of the average value of positive pore pressures.

The slope-averaged value of positive pore pressure decreased when the water level in the bedrock depression rose high enough so that water spilled over the bedrock ridge. This macro-scale spillage determined the second peak of the hydrograph after the end of the *long-rainfall* event (Figure 2), and the second peak of the variance  $\sigma_{\psi}^2(t)$  of the pore pressure values at the soil–bedrock interface observed after the end of the *long-rainfall* event (Figure 4(c)).

The dynamics of filling and spilling were strongly affected by the hillslope gradient. The fill and spill mechanism transitioned from a fill-dominated system at 13° to a spill-dominated system at 30°. The higher the hillslope gradient, the lower the spatial extension and temporal persistence of transient saturation at the soil–bedrock interface were (Figures 3 and 4(a)). While these general findings follow the hydrological analysis of Hopp and McDonnell (2009), our stability-based analysis showed that in the first phase of rainfall, the three investigated hillslope angles ( $\beta = 13^\circ$ ,  $\beta = 20^\circ$ ,  $\beta = 30^\circ$ ) exhibited similar patterns of pore-pressure. In this first phase, flow occurred only vertically through the soil profile because of the high vertical gradient of pressure head. The hydrological response of the three hillslope angles changed only in the second phase of the rainfall event, when the infiltration front reached the poorly permeable soil–bedrock interface where positive pore pressures then developed. As observed in many studies, the break in vertical permeability between soil and bedrock materials was a key driver for lateral flow generation (see early work by Weyman, 1973, and later review in Weiler *et al.*, 2006). This positive pore pressure development induced an increase in the hydraulic conductivity of two to three orders of magnitude at the soil–bedrock interface with a subsequent large increase in lateral flux. Torres *et al.* (1998) showed that this behavior is typical of coarse-soil with a steep, non-linear hydraulic conductivity function  $K(\psi)$  near zero pressure head. A very large increase in hydraulic conductivity and lateral flow is thus observed when a threshold suction head value is exceeded. This explains the very similar values of the variance of pressure head at the soil–bedrock interface observed during the early rainfall-hours for all the three hillslope gradients analyzed (Figure 4(c)), and

the subsequent different dynamics when the magnitude of lateral flow become strongly affected by the hillslope inclination.

### On the interaction of subsurface topography, hillslope hydrology and landslide triggering

The steepest hillslope (the modified 30°-Panola hillslope) was the only slope representation to exhibit failure during the investigated rainfall events. Unlike the 13°-Panola hillslope, spilling of water from the main bedrock depression at the 30°-Panola hillslope occurred during the same rainfall event (i.e. during the second phase of rainfall when lateral flows become relevant). This was basically related to the different velocity of the 30°-Panola hillslope in dissipating the positive pore pressure than the 13°-Panola hillslope.

Development of pressure head at the soil–bedrock interface during the second phase of rainfall (i.e. when lateral flows were first observed) was influenced by the bedrock microtopography. To show clearly how such microtopography influences these processes, we created within Hydrus 3-D a 30°-planar hillslope of identical dimension and mean soil depth as our study hillslope. Figure 8 illustrates and compares the near surface hydrological response of the two slopes where only the subsurface topography is different. Numerical simulation (with Hydrus 3-D) obtained by setting the same boundary and initial conditions as for the ‘irregular’ 30°-Panola hillslope showed that in the planar case (Figures 8(c) and 8(d)), a saturated wedge developed at the slope base and expanded upslope as described in Weyman (1973, 1974 and subsequent studies). This schematic representation (pore pressure head directly related to the upslope contributing area) underlies most of today’s topographic index-based landslide models (Montgomery and Dietrich, 1994; Borga *et al.*, 2002). The resulting slip surface then forms starting from the hillslope toe and propagates upslope.

On the other hand, transient saturation at the Panola (irregular) hillslope (Figure 8(a) and 8(b)) is accomplished via a combination of subsurface saturation in shallow soil areas and subsurface saturation in the bedrock depressions (located on the midslope). Maximum pore pressure increases are localized in the bedrock depression, where the factor of safety is then affected most. Unlike the synthetic, idealized planar slope, pore pressure fields on the irregular Panola hillslope are weakly correlated with the upslope contributing area calculated from the digital elevation model (DEM) of the bedrock surface. Interestingly, the failure zone was not localized in the main bedrock depression on the midslope where the maximum increase of pore pressure values were observed. Rather, it was located in the zone immediately upslope the main depression (Figure 6), where the localized bedrock surface was very steep and pore pressure increased enough to generate instability. Here, pore pressure increased because of the presence of the bedrock ridge just downslope the main bedrock depression that induced upslope flow accumulation. This result recalls findings of Speight (1980) who argued that it is the balance between the specific catchment area (i.e. upslope area) and the dispersal area (i.e. downslope area) that controls the ‘storage propensity’ of a given location. We argue that downslope topographic micro-relief can significantly modify the upslope flow dynamics, altering the drainage directions and determining the landslide position.

### Issues in modeling slope stability

The simulation effort reported in this study focused on a relatively small spatial scale (the ~0.1 ha Panola hillslope) and a relatively

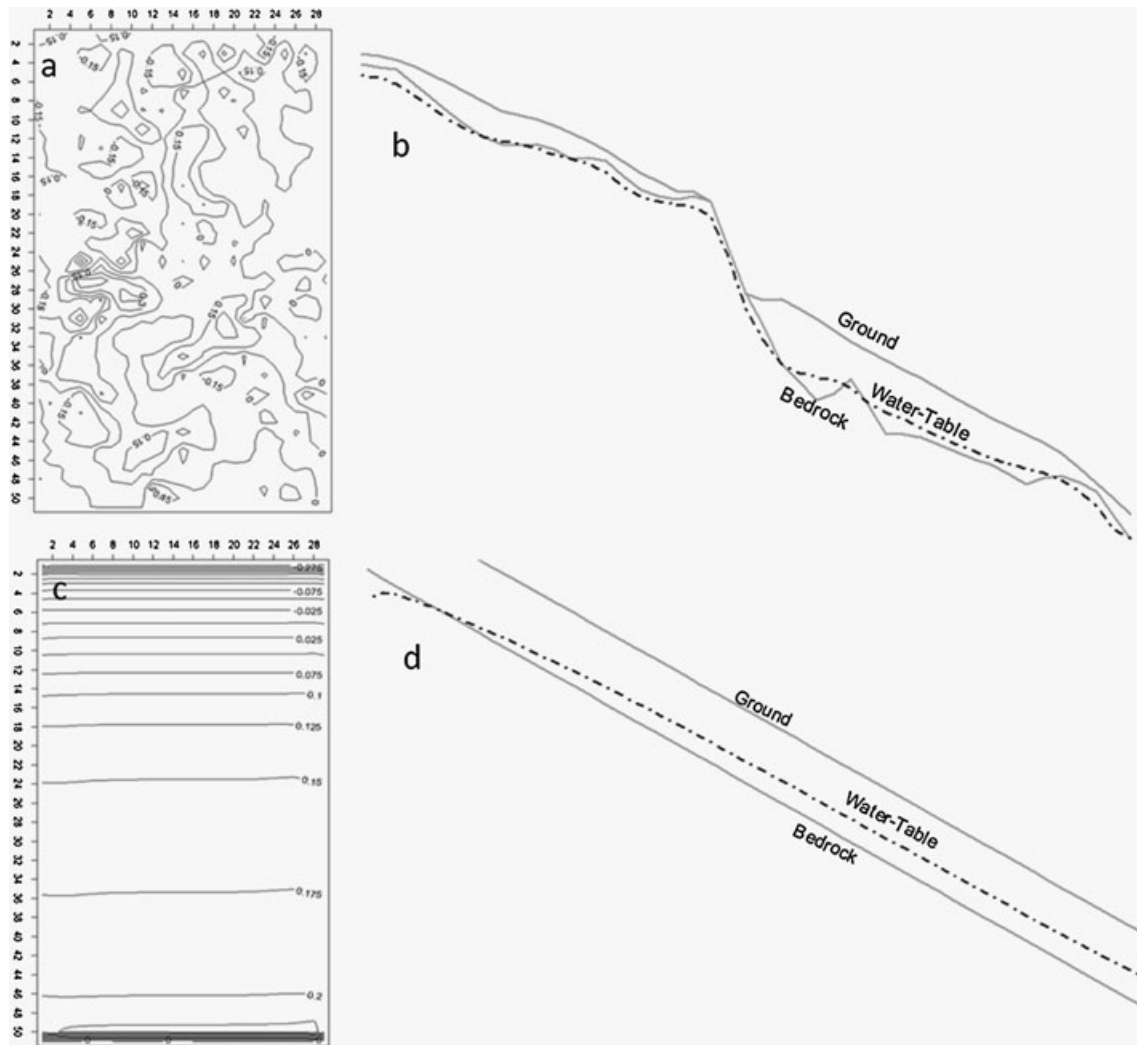


**Figure 8.** Comparison between the hydrological behavior of the ‘irregular’ Panola hillslope and a ‘regular’ planar hillslope. Both slopes received an input of  $6.25 \text{ mm h}^{-1}$  over 9 h. Panels (a) and (c) show the pressure head lines (at the 9th rainfall hour) at the soil–bedrock interface of the irregular and regular slopes, respectively. A saturated wedge expands upslope from the hillslope toe in the planar case (d). Roughness at the bedrock topography of the Panola hillslope (b) induce localized increase in pressure head (by preventing the free downslope drainage) resulting in complex patterns of instability. The vertical dimensions in panels (b) and (d) are exaggerated differently.

short temporal scale. To show the potential effect of subsurface topography in determining timing and position of shallow landslide initiation, we used a methodology which is similar to that of Dutton *et al.* (2005) and Mirus *et al.* (2007), with a ‘sophisticated’ three-dimensional hydrological analysis and separate FS estimates. Admittedly, this approach does not address the fully coupled processes of hydrologic response and slope deformation, which would be desirable to describe the complex mechanism of collapse induced by our irregular bedrock topography. A coupled model has been developed by Borja and White (2010). They developed a physics-based continuum model that captures the coupled solid deformation–fluid flow processes in variably saturated slopes. Their model accommodates relevant constitutive properties of the soil, in order to realistically quantify stresses and pore pressures responsible for triggering slope failure. In future studies, this will be the best approach to assess the role of bedrock depressions on soil displacements and subsequent slope failure. What makes this next step challenging is that this type of model requires a long list of further details on soil properties (in addition to those required by our uncoupled model), including: elastic bulk modulus, Poisson’s ratio (needed to introduce stresses in the model), dilatancy angle (that affects the volume change of the soil during yielding) and possibly other parameters depending on the constitutive law used to model the soil material. Furthermore, characterization of the initial *in situ* stress

conditions within the slope would be needed for implementation of such an approach.

Here, although not as rigorous as the hydrologic-response (Hydrus 3-D) model used in our study, our simplified slope stability model provided a first-order understanding of the importance of irregular bedrock topography in the context of hillslope stability. We used the infinite slope stability model to establish the triggered zones (or local instability), and then described the mechanical interactions among pixels by using the CA model. The rationale behind this is that landslide initiation requires that the equilibrium threshold is exceeded in a certain number of locations close to the triggered (and often isolated) points, in order to form a pattern of weakness for the soil mantled slope. The triggered points increase the shear stress in adjacent points in the hillslope causing failure of a connected domain with shear stress larger than the threshold value (Pelletier *et al.*, 1997). It should be noted that we did not provide a definitive value of the factor of safety for the connected domain (i.e. failure area). Indeed, our efforts aimed to understand the impact of the irregular subsurface topography in determining the spatial spreading and temporal development of this connected failure area (i.e. the threshold-like expansion behavior that emerged during the second phase of the rainfall).

We also tested a CA model with a different rule to propagate soil-stresses of destabilized cells; in this modified version, the



destabilizing force  $F_d^i$  of the unstable cell  $i$  is only redistributed to the neighbouring cells with lower elevation. Results by this modified CA model confirmed that instability spread over large area once about 35 mm threshold on cumulative rainfall was exceeded, and suggested that the fast spreading of instability is not dependent on the redistribution mechanism of soil stresses. However, we also found that the redistribution mechanism has a considerable effect on the final percentage of unstable area (8% of the hillslope area with the modified CA model, against ~25% provided by Equation (7) – see Figure 7), indicating that the redistribution rules in our CA model needs further investigation.

## Implications for catchment-scale shallow landslide models

Many recent catchment-scale landslide modeling efforts have focused on new and more effective ways to describe flows from upslope by using the topographic index or dynamic topographic index approaches (i.e. Montgomery and Dietrich, 1994; Tarolli and Tarboton, 2006). Our work suggests that new focus on soil depth mapping (to then back-calculate the topography of the bedrock surface) may be useful to improve our ability to predict timing and location of shallow landslide initiation and that subsurface topography has a strong impact in controlling the connectivity of saturated patches at the soil–bedrock interface. However, despite this evidence, most catchment-scale shallow landslide models fail to include a connectivity component for subsurface hydrological connectivity. Thus, we invoke at least a simplified treatment of the problem. This has been done for overland flow processes (Lane *et al.*, 2004) and fine sediment and soil erosion processes (Reid *et al.*, 2007; Lane *et al.*, 2009) by extending the traditional topographic index approach to include a simplified representation of surface hydrological connectivity. A similar approach can be adopted for subsurface flow processes and shallow landslide processes. Research to pursue this objective is currently underway (Lanni *et al.*, 2012).

## Conclusions

This paper has sought to link an important new finding from the hillslope hydrological literature – the filling and spilling of transient saturation at the soil–bedrock interface – with landslide related processes at the hillslope scale. We found that bedrock depressions play a key role in pore pressure dynamics and shallow failure initiation. Topographic depressions at the bedrock layer induce localized zones of increased pressure head such that the development of pore-pressure fields—not predictable by ground surface topography—leads to rapid landslide propagation. Isolated transient groundwater pockets at the soil–bedrock interface produced during rainfall events spill over small bedrock ridges to form sudden and connected saturated areas that instantaneously reduce the factor of safety through the hillslope. This emergent behavior occurs after a precipitation threshold has been exceeded and may be responsible for the rapid transition from stable to unstable conditions generally observed for shallow (and for this unpredictable) landslide phenomena.

Modeling pore pressure spatial distribution using the topography of the bedrock may significantly improve the ability of landslide models to detect shape and location of the slip surface. While such data are largely unavailable, except for well studied hillslopes and watersheds, promising new work (Pelletier and Rasmussen, 2009) suggests that soil depth

modeling may be a way to then derive bedrock topographic relief and lead to the coupling of physically-based landslide models with quantitative soil–landscape methods to ultimately improve our ability to predict shallow landslide potential.

*Acknowledgements*—We thank the many Panola field staff for their collection of the original Panola data, including Jim Freer, Doug Burns, Al Zumbuhl, Ilja Tromp-van Meerveld. Jake Peters and the USGS Panola staff are thanked for their ongoing support of the site and our work. Tim Burt, Greg Hancock, Mark Reid, and Jonathan Godt are thanked for useful early discussions. We are grateful to the two anonymous reviewers for comments that improved the quality of this manuscript.

## References

- Arnone E, Noto LV, Lepore C, Bras RL. 2011. Physically-based and distributed approach to analyze rainfall-triggered landslides at watershed scale. *Geomorphology* **133**: 121–131.
- Avolio MV, Di Gregorio S, Mantovani F, Pasuto A, Rongo R, Silvano S, Spataro W. 2000. Simulation of the 1992 Tessina landslide by a cellular automata model and future hazard scenarios. *JAG* **2**: 41–50.
- Bak P, Tang C, Wiesenfeld K. 1987. Self-organized criticality: an explanation of  $1/f$  noise. *Physical Review Letters* **147**: 297–300.
- Baum RL, Savage WZ, Godt JW. 2008. TRIGRS – A FORTRAN program for transient rainfall infiltration and grid based regional slope stability analysis, version 2.0. US Geological Survey Open File Report 2008 1159, 74.
- Baum RL, Godt JW, Savage, WZ. 2010. Estimating the timing and location of shallow rainfall-induced landslides using a model for transient, unsaturated infiltration. *Journal of Geophysical Research* **115**. DOI: 10.1029/2009JF001321.
- Bishop AW. 1959. The principle of effective stress. *Tek Ukebl* **106**(39): 859–863.
- Borga M, Dalla Fontana G, Cazorzi F. 2002. Analysis of topographic and climatologic control on rainfall-triggered shallow landsliding using a quasi-dynamic wetness index. *Journal of Hydrology* **268**: 56–71.
- Borja RI, White JA. 2010. Continuum deformation and stability analyses of a steep hillside slope under rainfall infiltration. *Acta Geotechnica* **5**: 1–14. DOI: 10.1007/s11440-009-0108-1.
- Buttle JM, Dillon PJ, Eerkes GR. 2004. Hydrologic coupling of slopes, riparian zones and streams: an example from the Canadian Shield. *Journal of Hydrology* **287**(1–4): 161–177. DOI: 10.1016/j.jhydrol.2003.09.022.
- Campos TMP, Andrade MHN, Gerscovich DMS, Vargas Jr. EA. 1994. Analysis of the failure of an unsaturated gneissic residual soil slope in Rio de Janeiro, Brazil. 1st Panamerican Symposium On Landslides, pp. 201–213.
- Casadei M, Dietrich WE, Miller NL. 2003. Testing a model for predicting the timing and location of shallow landslide initiation in soil-mantled landscapes. *Earth Surface Processes and Landforms* **28**: 925–950. DOI: 10.1002/esp.470.
- Clerici A, Perego S. 2000. Simulation of the Parma River blockage by the Corniglio landslide (Northern Italy). *Geomorphology* **33**: 1–23.
- D'Ambrosio D, Di Gregorio S, Iovine G, Lupiano V, Rongo R, Spataro W. 2003. First simulations of the Sarno debris flows through cellular automata modeling. *Geomorphology* **54**: 91–117.
- Dietrich WE, McKean J, Bellugi D, Perron T. 2007. The prediction of shallow landslide location and size using a multidimensional landslide analysis in a digital terrain model. Proceedings of the Fourth International Conference on Debris-Flow Hazards Mitigation: Mechanics, Prediction, and Assessment (DFHM-4); Chengdu, China.
- D'Odorico P, Fagherazzi S, Rigon R. 2005. Potential for landsliding: dependence on hypsograph characteristics. *Journal of Geophysical Research* **110**. DOI: 10.1029/2004JF000127.
- Duan J, Grant GE. 2000. Shallow landslide delineation for steep forest watersheds based on topographic attributes and probability analysis. *Terrain Analysis: Principles and Applications*, Wilson JP, Gallant JC (eds). New York. 311–329.
- Dutton A, Loague K, Wemple BC. 2005. Simulated effect of a forest road on near-surface hydrologic response and slope stability. *Earth Surface Processes and Landforms* **30**: 325–338.

- Fredlund DG, Rahardjo H. 1993. *Soil Mechanics for Unsaturated Soils*. Wiley-Interscience: New York.
- Freer J, McDonnell JJ, Beven KJ, Peters NE, Burns DA, Hooper RP, Aulenbach B, Kendall C. 2002. The role of bedrock topography on subsurface storm flow. *Water Resources Research* **38**: 1269.
- van Genuchten MT. 1980. A closed-form equation for predicting the hydraulic conductivity of unsaturated soils. *Soil Science Society of America Journal* **44**: 892–898.
- Glade T. 1998. Establishing the frequency and magnitude of landslide-triggering rainstorm events in New Zealand. *Environmental Geology* **35**: 2–3.
- Godt JW, Baum RL, Lu N. 2009. Using soil suction and moisture content measurements for landslide prediction. *Geophysical Research Letters* **36**: L02403. DOI: 10.1029/2008GL035996.
- Graham CB, Woods RA, McDonnell JJ. 2010. Hillslope threshold response to rainfall: (1) a field based forensic approach. *Journal of Hydrology* **393**(1–2): 65–76. DOI: 10.1016/j.jhydrol.2009.12.015.
- Guthrie RH, Deadman PJ, Cabrera AR, Evans SG. 2007. Exploring the magnitude–frequency distribution: a cellular automata model for landslides. *Landslides* **5**: 151–159. DOI: 10.1007/s10346-007-0104-1.
- Hawke R, McConchie J. 2009. In situ measurement of soil moisture and pore-water pressures in an ‘incipient’ landslide: Lake Tutira, New Zealand. *Journal of Environmental Management* **92**(2).
- Hjerdt KN, McDonnell JJ, Seibert J, Rodhe A. 2004. A new topographic index to quantify downslope controls on local drainage. *Water Resource Research* **40**: W05602. DOI: 10.1029/2004WR003130.
- Hopp L, McDonnell JJ. 2009. Connectivity at the hillslope scale: identifying interactions between storm size, bedrock permeability, slope angle and soil depth. *Journal of Hydrology* **376**(3–4): 378–391. DOI: 10.1016/j.jhydrol.2009.07.047.
- Iovine G, Di Gregorio S, Lupiano V. 2003. Debris-flow susceptibility assessment through cellular automata modeling: an example from 15–16 December 1999 disaster at Cervinara and San Martino Valle Caudina (Campania, southern Italy). *Natural Hazards Earth Systems Science* **3**: 457–468.
- Iverson RM, Reid ME, LaHusen RG. 1997. Debris-flow mobilization from landslides. *Annual Review of Earth Planet Science* **25**: 85–138.
- Jensen JH. 1998. *Self-Organized Criticality*. Cambridge University Press: Cambridge.
- Lane SN, Brookes CJ, Kirkby MJ, Holden J. 2004. A network index based version of TOPMODEL for use with high-resolution digital topographic data. *Hydrological Processes* **18**: 191–201. DOI:10.1002/hyp.5208.
- Lane SN, Reaney SM, Heathwaite AL. 2009. Representation of landscape hydrological connectivity using a topographically driven surface flow index. *Water Resource Research* **45**: W08423. DOI: 10.1029/2008WR007336.
- Lanni C, Borga M, Rigon R, Tarolli P. 2012. Modelling catchment-scale shallow landslide occurrence by means of a subsurface flow path connectivity index. *Hydrological Earth Systems Science Discussion* **9**: 4101–4134. www.hydrolog-earth-syst-sci-discuss.net/9/4101/2012/doi:10.5194/hessd-9-4101-2012
- Lu N, Godt JW. 2008. Infinite-slope stability under steady unsaturated conditions. *Water Resource Research* **44**: W11404. DOI: 10.1029/2008WR006976.
- Lu N, Likos WJ. 2006. Suction stress characteristic curve for unsaturated soil. *Journal of Geotechnical and Geoenvironmental Engineering* **132**: 131–142.
- Minder JR, Roe GH, Montgomery DR. 2009. Spatial patterns of rainfall and shallow landslide susceptibility. *Water Resource Research* **45**: W04419. DOI: 10.1029/2008WR007027.
- Mirus BB, Ebel BA, Loague K, Wemple BC. 2007. Simulated effect of a forest road on near surface hydrologic response. *Earth Surface Processes and Landforms* **32**: 126–142. DOI: 10.1002/esp.1387.
- Montgomery DR, Dietrich WE. 1994. A physically based model for the topographic control on shallow landsliding. *Water Resources Research* **30**(4): 1153–1171.
- NOAA. 1991. Local climatological data, annual summary with comparative data, 1990, Atlanta, Georgia, Asheville, N.C., 6.
- Olshansky R. 1990. Landslide hazard in the United States. *Case Studies in Planning and Policy Development*. Garland Publishing: New York 178.
- Pack RT, Tarboton DG, Goodwin CN. 1998. The SINMAP approach to terrain stability mapping. In *Proceedings – International Congress of the International Association for Engineering Geology and the Environment 8*, Vol. 2, Moore DP, Hungr O (eds). A.A. Balkema: Rotterdam, Netherlands; 1157–1165.
- Pelletier JD, Rasmussen C. 2009. Geomorphically-based predictive mapping of soil thickness in upland watersheds. *Water Resources Research* **45**. DOI: 10.1029/2008WR007319.
- Pelletier JD, Malamud BD, Blodgett T, Turcotte DL. 1997. Scale-invariance of soil moisture variability and its implications for the frequency-size distribution of landslides. *Engineering Geology* **48**(3–4): 255–268.
- Piegari E, Di Maio R, Milano, L. 2009. Characteristic scales in landslide modeling. *Nonlinear Processes in Geophysics* **16**: 515–523. DOI: 10.5194/npg-16-515-2009.
- Reid, SC, Lane SN, Montgomery DR, Brookes CJ. 2007. Does hydrological connectivity improve identification of coarse sediment delivery in upland environments? *Geomorphology* **90**: 263–282.
- Richards LA. 1931. Capillary conduction of liquids in porous mediums. *Physics* **1**: 318–333.
- Rodriguez-Iturbe I, Rinaldo A. 1997. *Fractal River Networks: Chance and Self-Organization*. Cambridge University Press: New York.
- Savage WZ, Godt JW, Baum RL. 2004. Modeling time-dependent areal slope stability. In *Landslides: Evaluation and Stabilization*, Lacerda WA, Ehrlich M, Fontoura SAB, Sayao ASF (eds). Taylor and Francis Group: London; 23–36.
- Schmidt KM, Roering JJ, Stock JD, Dietrich WE, Montgomery DR, Schaub T. 2001. The variability of root cohesion as an influence on shallow landslide susceptibility in the Oregon Coast Range. *Canadian Geotechnical Journal* **38**(5): 995–1024.
- Schuster RL. 1995. Keynote paper: recent advances in slope stabilization. In *Landslides – Glissements de terrain*, Bell H (ed). Balkema: Rotterdam, 1715–1745.
- Simoni S, Zanotti F, Bertoldi G, Rigon R. 2008. Modelling the probability of occurrence of shallow landslides and channelized debris flows using GEOTOP-FS. *Hydrological Processes* **22**(4): 532–545.
- Simunek J, van Genuchten MT, Sejna M. 2006. The HYDRUS Software Package for Simulating Two- and Three-dimensional Movement of Water, Heat, and Multiple Solutes in Variably-Saturated Media: Technical Manual. Version 1.0. PC-Progress, Prague, Czech Republic.
- Speight JG. 1980. The role of topography in controlling throughflow generation: a discussion. *Earth Surface and Processes* **5**: 187–191.
- Spence C. 2010. A paradigm shift in hydrology: storage thresholds across scales influence catchment runoff generation. *Geography Compass* **4**: 819–833. DOI: 10.1111/j.1749-8198.2010.00341.x.
- Spence C, Woo Ming-ko. 2003. Hydrology of subarctic Canadian shield: soil-filled valleys. *Journal of Hydrology* **279**(1–4): 151–166. DOI: 10.1016/S0022-1694(03)00175-6.
- Tarolli P, Tarboton DG. 2006. A new method for determination of most likely landslide initiation points and the evaluation of digital terrain model scale in terrain stability mapping. *Hydrological Earth Systems Science* **10**: 663–677. DOI: 10.5194/hess-10-663-2006.
- Terzaghi K. 1943. *Theoretical Soil Mechanics*. John Wiley and Sons: New York.
- Terzaghi K, Peck RB, Mesri G. 1996. *Soil Mechanics in Engineering Practice*. Wiley: New York.
- Torres R, Dietrich WE, Montgomery DR, Anderson SP, Loague KM. 1998. Unsaturated zone processes and the hydrologic response of a steep, unchanneled catchment. *Water Resources Research* **34**(8): 1865–1879.
- Tromp-van Meerveld HJ, McDonnell JJ. 2006a. Threshold relations in subsurface stormflow: 1. A 147-storm analysis of the Panola hillslope. *Water Resource Research* **42**, W02410. DOI: 10.1029/2004WR003778.
- Tromp-van Meerveld HJ, McDonnell JJ. 2006b. Threshold relations in subsurface stormflow: 2. The fill and spill hypothesis. *Water Resources Research* **42**, W02411. DOI: 10.1029/2004WR003800.
- Tromp-van Meerveld HJ, Peters NE, McDonnell JJ. 2007. Effect of bedrock permeability on subsurface stormflow and the water balance of a trenched hillslope at the Panola Mountain Research Watershed, Georgia, USA. *Hydrological Processes* **21**: 750–769.
- Turcotte DL, Malamud BD, Guzzetti F, Reichenbach P. 2002. Self-organization, the cascade model, and natural hazards. *Proceedings of the National Academy of Science USA* **19**: 2530–2537.
- Van Beek R. 2002. Assessment of the influence of changes in climate and land use on landslide activity in a Mediterranean environment. Netherlands Geographical Studies no. 294, KNAG, Faculty of Geosciences, Utrecht University, 366.

- Vanapalli SK, Fredlund DG, Pufahl DE, Clifton AW. 1996. Model for the prediction of shear strength with respect to soil suction. *Canadian Geotechnical Journal* **33**(3): 379–392. DOI: 10.1139/t96-060.
- Weiler M, McDonnell JJ. 2004. Virtual experiments: a new approach for improving process conceptualization in hillslope hydrology. *Journal of Hydrology* **285**: 3–18.
- Weiler M, McDonnell JJ, Tromp-van Meerveld I, Uchida T. 2006. Subsurface stormflow. *Encyclopedia of Hydrological Sciences*. DOI: 10.1002/0470848944.hsa119.
- Weyman DR. 1973. Measurements of the downslope flow of water in a soil. *Journal of Hydrology* **20**(3): 267–288. DOI: 10.1016/0022-1694(73)90065-6.
- Weyman DR. 1974. Runoff processes, contributing area and streamflow in a small upland catchment. In *Fluvial Processes in Instrumented Watersheds*, Gregory KJ, Walling DE (eds). Institute of British Geographers: London; 33–43.
- Wu W, Sidle R. 1995. A distributed slope stability model for steep forested basins. *Water Resources Research* **31**: 2097–2110.